1 **Kinesin-2 from *C. reinhardtii* is an atypically fast and auto-inhibited motor that is**

2 **activated by heterotrimerization for intraflagellar transport**

3

4 Punam Sonar[1], Wiphu Youyen[2], Augustine Cleetus[1], Pattipong Wisanpitayakorn[3], Iman

5 S. Mousavi[2], Willi L. Stepp[1], William O. Hancock[4], Erkan Tüzel[3], and Zeynep Ökten[1]*

6

7 [1]Physik Department E22, Technische Universität München, Garching, Germany.

8 [2]Department of Physics, Worcester Polytechnic Institute, 100 Institute Road, Worcester,

9 Massachusetts.

10 [3]Bioengineering Department, College of Engineering, Temple University, Philadelphia,

11 Pennsylvania.

12 [4]Department of Biomedical Engineering, Pennsylvania State University, University Park, PA

13 16802, USA.

14 [1*]Physik Department E22, Technische Universität München, Garching, Germany.

15 zoekten@ph.tum.de.

16

17 **Key words:** Intraflagellar Transport, cilia, flagella, *C. reinhardtii*, *C. elegans*, motor

18 cooperation

19

Summary

The construction and function of virtually all cilia require the universally conserved
process of Intraflagellar Transport (IFT) [1, 2]. During the atypically fast IFT in the green
alga *C. reinhardtii*, up to ten kinesin-2 motors 'line up' in a tight assembly on the trains [3],
provoking the question of how these motors coordinate their action to ensure smooth and
fast transport along the flagellum without standing in each other's way. Here, we show
that the heterodimeric FLA8/10 kinesin-2 alone is responsible for the atypically fast IFT in
C. reinhardtii. Notably, in single-molecule studies, FLA8/10 moved at speeds matching
those of *in vivo* IFT [4], but additionally displayed a slow velocity distribution, indicative of
auto-inhibition. Addition of the KAP subunit to generate the heterotrimeric FLA8/10/KAP
relieved this inhibition, thus providing a mechanistic rationale for heterotrimerization with
the KAP subunit in fully activating FLA8/10 for IFT *in vivo*. Finally, we link fast FLA8/10
and slow KLP11/20 kinesin-2 from *C. reinhardtii* and *C. elegans* through a DNA tether to
understand the molecular underpinnings of motor coordination during IFT *in vivo*. For
motor pairs from both species, the co-transport velocities very nearly matched the single-
molecule velocities, and the complexes both spent roughly 80% of the time with only one
of the two motors attached to the microtubule. Thus, irrespective of phylogeny and kinetic
properties, kinesin-2 motors prefer to work alone without sacrificing efficiency. Our
findings thus offer a simple mechanism for how efficient IFT is achieved across diverse
organisms despite being carried out by motors with different properties.

40   Cilia or flagella (used interchangeably) are microtubule-based organelles that project from

41   the surface of most eukaryotic cells. As evidenced from their remarkably diverse

42   deployment across eukaryotes, they are among the most evolutionarily adaptive of all

43   organelles. This diversity is manifested as the large number of seemingly unrelated

44   human disorders linked to impaired ciliary biogenesis, ranging from infertility to vision

45   degeneration [5-12]. Such functional diversity starkly contrasts with the highly conserved

46   nature of IFT, the process that builds and maintains virtually all cilia from unicellular

47   organisms up to humans. IFT was first observed in the unicellular green alga *C. reinhardtii*

48   as movement of large, non-membrane-bound 'trains' between the ciliary tip and base

49   (Figure 1) [13]. Given that these trains moved on axonemes – an elaborate microtubule-

50   based scaffold – it soon became clear that IFT is powered by cilia-specific kinesin-2 and

51   dynein-2 motors [1, 14-21]. The kinesin-2 motors that carry out IFT appear to have co-

52   evolved with the axonemal structure, suggesting that their mechanochemical properties

53   are adapted to the highly specialized ciliary environment [22, 23]. Unlike most kinesins

54   that form homodimers, the canonical ciliary kinesin-2 FLA8/FLA10/KAP in *C. reinhardtii*

55   is a heterotrimeric complex consisting of two distinct motor subunits and an accessory,

56   non-motor subunit [4, 14, 24, 25]. Indeed, heterotrimerization of the kinesin-2 motor with

57   the KAP subunit proved to be a universally required property of IFT from the unicellular

58   *C. reinhardtii* up to mammals [23, 25-28]. KAP is suggested to serve as a cargo adaptor

59   for the kinesin-2 motor, however, the physiological relevance of heterotrimerization

60   remains unclear [23].

61

62   Curiously, although kinesin-2-driven IFT trains in *C. reinhardtii* move with a velocity of

63   ~2000 nm/s [4], all subsequently characterized heteromeric kinesin-2 motors from diverse

64   model organisms move roughly four-fold slower, both *in vivo* and *in vitro* [27, 29-34]. What

65   is not known is whether FLA8/10 motors display such atypically high velocities in isolation,

66   or whether the fast IFT speeds result from cooperative effects of the assembled motor

67   groups in the *C. reinhardtii* model. Consistent with this notion, functional studies with the

68   *C. reinhardtii* flagellum estimated that up to ten kinesin-2 and dynein-2 motors are

69   reciprocally engaged to move the IFT trains either towards the tip or the base of the cilium,

70   respectively [3]. Given an average train size of ~200 nm [35], transport toward the ciliary

71 tip thus involves up to 20 active kinesin-2 head domains that 'line up' along the train with

72 close spacing between dimers. Moreover, these kinesin-2 motors were shown to

73 exclusively use the B-tubule of the microtubule-doublet of the axoneme, which prevents

74 head-on collisions with retrograde trains moving along the A-tubulin [35]. Such

75 specialized transport geometry raises the question of how the assembled head domains

76 on each train coordinate their actions to achieve efficient IFT *in vivo* (Figure 1).
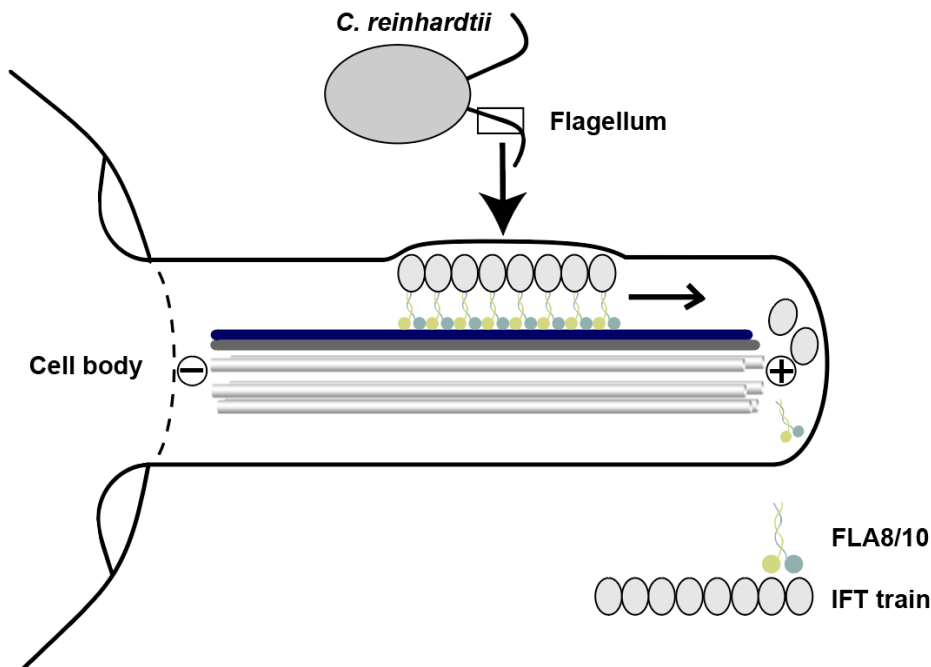
77

78 **Figure 1: Schematics of kinesin-2-driven IFT in *C. reinhardtii*.** Linear arrays of IFT particles or 'trains'

79 are transported towards the plus-end of the axoneme. This kinesin-2-driven anterograde transport takes

80 place on the B-tubule of the microtubule doublet (highlighted in blue), leaving the A-tubule (highlighted in

81 dark gray) for the dynein-2 driven IFT towards the minus-end of the axonemes (not shown).

82

83 In contrast to the kinesin/dynein-driven bi-directional transport of cargo in the cytoplasm,

84 which displays frequent reversals, IFT trains move without interruption, out to the ciliary

85 tip via kinesin-2, or back to the base via dynein-2 [2, 36, 37]. This behavior suggests that

86 the oppositely directed kinesin-2 and dynein-2 motors are activated reciprocally during

87 IFT. In support, recent cryo-EM studies with the *C. reinhardtii* flagellum provide

88 compelling evidence that kinesin-2-driven IFT trains transport the minus-end directed

89 dynein-2 as inactive cargo towards the ciliary tip [38]. The underlying molecular

90 mechanisms of how kinesin-2 and dynein-2 motors are specifically activated and inhibited

91 during IFT remain largely unknown. It is conceivable that heterodimeric kinesin-2 also

92 requires an adaptor to be recruited and activated for IFT, as previously demonstrated with

93 the homodimeric OSM-3 kinesin-2 from the *C. elegans* model [39].

94   Here we turned to *in vitro* reconstitution assays and *in silico* simulations to address

95   following questions. Is the heterodimeric FLA8/10 motor from *C. reinhardtii* alone

96   sufficient to explain the atypically fast IFT velocity of 2000 nm/s *in vivo* [13], or does the

97   fast speed result from the collective motor behaviors? Second, how do populations of

98   FLA8/10 motors coordinate their actions to achieve the smooth and continuous transport

99   observed *in vivo*? Lastly, how are FLA8/10 motors activated and inhibited during IFT?

100

101   To gain a mechanistic understanding of *C. reinhardtii* IFT, we recombinantly expressed

102   the FLA8 and FLA10 subunits of the heterotrimeric kinesin-2. The Flag-tagged FLA8

103   subunit robustly co-precipitated the 6XHis-tagged FLA10, demonstrating the specific

104   heterodimerization between the two different motor subunits (Figure S1A). Next, we

105   turned to functional single-molecule and multiple-motor filament gliding assays to

106   investigate whether a single FLA8/10 motor can move processively on surface-attached

107   microtubules, and if so, whether the single motor speeds differ from the speed of motors

108   working in ensembles.

109   To this end, we labeled the SNAP-tag on the FLA10 subunit with a fluorescent dye and

110   tracked the movement of single fluorescently labeled motors (Figure 2A). The

111   heterodimeric FLA8/10 motors not only moved processively but also displayed two

112   velocity populations (Figure 2A). The faster velocity population at ~2000 nm/s

113   demonstrates that this heterodimeric FLA8/10 motor from *C. reinhardtii* alone is sufficient

114   to achieve the atypically fast kinesin-2-dependent IFT velocities observed *in vivo* [13].

115   The slower velocity population, centered around 1000 nm/s, suggests that, like other full-

116   length kinesins [4, 40-44], this motor is capable of auto-inhibition.

117   In other kinesins, folding of the distal C-terminal 'tail' domain onto the N-terminal catalytic

118   heads suppresses the ATPase activity of the dimeric motor, and attaching motors to a

119   surface via their C-terminal tail domains in multiple-motor filament gliding assays relieves

120   this inhibition [29, 30]. Consistent with this, we observed consistently fast velocities in

121   multiple-motor assays (Figure S2A, left, Suppl. movie 1). Thus, the atypically fast IFT

122   velocities in *C. reinhardtii* do not result from collective motor behaviors, but instead are

123   inherent and unique to the FLA8/10 kinesin-2 motor (Figure 2A vs Figure S2A, left).

124   Additionally, a subset of our recombinant full-length FLA8/10 heterodimers are auto-

125   inhibited, likely through autoinhibitory folding of the tail domains onto the head domains.

126

127   Intrigued by the sub-population of inhibited motors (Figure 2A), we next asked whether

128   heterotrimerization with KAP may directly alter the activation state of FLA8/10. Previous

129   *in vivo* investigations with *C. reinhardtii* showed that the KAP subunit is required both for

130   achieving efficient processive movement of anterograde IFT trains, and for proper

131   targeting of the kinesin-2 motor to the ciliary base [25]. Consistent with this, assembling

132   the motor subunits into the heterotrimeric FLA8/10/KAP complex (Figure S1B) completely

133   abolished the auto-inhibition, and resulted in all motor complexes moving at full speed

134   (Figures 2A vs 2B). The ability of the KAP subunit to activate the FLA8/10 motor provides

135   a first mechanistic rationale for the assembly of the physiologically-relevant heterotrimeric

136   motor complex *in vivo* and underscores the importance of KAP in the efficient activation

137   of the FLA8/10 motor. The role of the KAP subunit in recruiting [25] and activating *C.*

138   *reinhardtii* FLA8/10 (Figure 2B) is conceptually highly similar to the adaptor-dependent

139   recruitment and activation of the homodimeric kinesin-2, OSM-3, that carries out IFT in

140   *C. elegans* [39, 45].

141

142   Because catalytic head domains are particularly well-conserved across the kinesin-2

143   family, a mechanistic explanation for the pronounced kinesin-2 speed differences

144   between the single-celled *C. reinhardtii* (~2000 nm/s) and multicellular organisms (~500

145   nm/s) is not immediately obvious [29-31, 33, 34, 46]. Intrigued by these findings, we next

146   asked whether we can delineate the domain responsible for the observed kinetic

147   differences between the respective model organisms. To this end, we replaced the KLP11

148   and KLP20 head domains in the KLP11/20 heterodimer [29] with the corresponding

149   FLA10 and FLA8 head domains respectively (Figure S2B). Strikingly, this chimeric motor

150   was not only active but also displayed a velocity of >1700 nm/s. Thus, the catalytic heads

151   and not sequences in the coiled-coil or tail domains are the main determinants of the

152   atypically fast kinesin-2-driven IFT velocity in *C. reinhardtii* (Figure S2B).
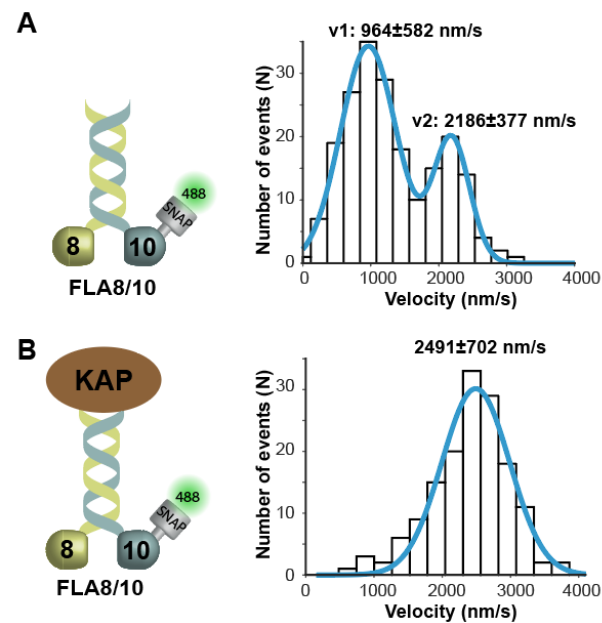
153

Figure 2: Full-length heterodimeric FLA8/10 is an atypically fast and auto-inhibited kinesin-2 motor.

(A) Left panel illustrates the wild type FLA8/10 motor that was tracked via the fluorescently labeled N-terminal SNAP-tag on the FLA10 subunit. Single motors displayed two distinct velocity distributions (v1= 964±582 nm/s and v2= 2186±377 nm/s (N=202)) with the fast v2 corresponding to the *in vivo* anterograde transport velocity in *C. reinhardtii* [13] and the slow v1 to auto-inhibition of the wild type FLA8/10 motor, respectively. **(B)** Left panel depicts the heterotrimeric FLA8/10/KAP complex that was tracked via fluorescently labeled SNAP-tag on the N-terminus of the FLA10 subunit. Addition of the KAP subunit abolished the slow velocity distribution (v1) that is observed with the wild type FLA8/10 (A), and the heterotrimeric FLA8/10/KAP complex displayed a fast velocity of 2491±702 nm/s (N=151). Data is fitted to a Gaussian distribution (±width of distribution, from two independent experiments).

We next turned to the more complex question of how the multiple kinesin-2 motors that line up in close proximity along each train (Figure 1), cooperate during IFT. To mimic this multi-motor transport *in vitro*, we used double-stranded DNA (dsDNA) to couple two kinesin-2 motors, i.e. four head domains, in close proximity (Figure S3). Given that the FLA8/10 motor is partially auto-inhibited (Figure 2A), we turned to protein engineering to create a fast and fully active kinesin-2 that matches the active anterograde transport motors *in vivo*. To this end, we replaced the FLA10 head with the FLA8 head domain, resulting in FLA8/8 that was heterodimerized by the FLA8 and FLA10 stalks. This chimeric motor no longer displayed the auto-inhibited population seen with the FLA8/10 (Figure 2A), and moved with fast velocities of >2000 nm/s in both single-molecule assays and multiple-motor filament gliding assays (Figure S2A, middle and Figure S2C). In contrast, replacing the FLA8 with the FLA10 head resulted in a chimeric FLA10/10 motor that was considerably slower than the FLA8/8 chimera (Figure S2A, middle vs right),

179   though still substantially faster than IFT kinesin-2 from *C. elegans* and other multicellular

180   organisms [29, 31-34, 46]. Thus, the fast speed of *C. reinhardtii* FLA8/10 cannot be

181   explained by differing activities of the two heads somehow combining to achieve fast

182   transport; instead, the fast speeds are a property of each head individually. *C. elegans*

183   KLP11/20 also combines a faster KLP20 with a slower KLP11 head [29], indicating that,

184   despite being distantly related, the unicellular *C. reinhardtii* and the multicellular *C.*

185   *elegans* share conceptual similarities. However, possessing different kinetic signatures

186   between the two heterodimerized heads is insufficient to explain the substantial velocity

187   differences between the two model organisms.

188

189   To examine whether the fast *C. reinhardtii* and the slow *C. elegans* kinesin-2 IFT motors

190   differ in their abilities to cooperate during multi-motor transport of IFT trains, we compared

191   the co-transport behaviors of the constitutively activated *C. reinhardtii* FLA8/8 (Figure

192   S2C) with that of *C. elegans* KLP11/20 [29]. The heterodimeric nature of kinesin-2

193   allowed for a well-defined and highly specific coupling and fluorophore labeling of the two

194   motors. Specifically, we introduced a N-terminal SNAP-(for fluorophore labeling) and C-

195   terminal Halo-tag (for dsDNA coupling) into the FLA8 subunit, respectively. The co-

196   expression of this functionalized FLA8 subunit with the chimeric FLA8^{head}FLA10^{stalk} motor

197   resulted in a kinesin-2 motor with the N-terminal SNAP- and C-terminal Halo-Tag on *one*

198   subunit only (Figure S3A). Next, we functionalized dsDNA, containing thiol groups at both

199   ends, to the Halo Iodoacetamide O4 ligand, which covalently links to Halo-Tags (Figure

200   S3B and S3C, see Supplementary Information for details). With this strategy, coupled

201   kinesin pairs were generated by covalently linking motors with C-terminal Halo-Tags to

202   each Iodoacetamide-functionalized end of the dsDNA [47, 48]. To ensure that only

203   coupled motor pairs are analyzed, motors were labeled on their N-terminal SNAP-tag with

204   different fluorophores as illustrated in Figure S3A. Simply mixing the two differentially

205   labeled FLA8/8 motors with the bi-functionalized dsDNA resulted in motor-DNA hybrids

206   (FLA8/8-FLA8/8 hereafter) that could be distinguished in *in vitro* reconstitution assays by

207   the movement of co-localized green and red fluorophores (Figure S3D, Suppl. movie 2).

208   Using the same strategy, we also coupled two constitutively activated KLP11/20 motors

209   from *C. elegans* for direct comparison [29] (KLP11/20-KLP11/20 hereafter) (Figure S3E,

210   Suppl. movie 3). Collectively, the heterodimeric nature of kinesin-2 allowed a highly stable

211   and specific DNA-motor coupling and fluorescent labeling with the respective

212   functionalization being unambiguously assigned to the subunits (Figures S4 and S5).

213

214   To gain mechanistic insight into the forces generated and the degree of inter-motor

215   coordination during co-transport by FLA8/8 and KLP11/20 motor pairs, we developed

216   coarse-grained simulations of motor stepping, described fully in Materials and Methods.

217   Briefly, motors are modeled as stochastic steppers and the motor-DNA complex is

218   modeled mechanically as a Freely Jointed Chain (FJC), with segments corresponding to

219   distinct sub-domains of the complex (Figure 3A). The two dimeric motors bind and unbind

220   from the microtubule at specified rates and when one motor detaches from the

221   microtubule, it is subjected to Brownian (Figure S6A) and entropic restoring forces from

222   the FJC linkage (Figure S6B). Motors step along the microtubule with a linear force-

223   velocity profiles and a 6 pN stall force (Figure S7A). Unloaded motor detachment rates

224   were calculated from experimental single-molecule run lengths and velocities

225   summarized in Tables S1 and S2. In this model, FLA8/8 and KLP11/20 are assumed to

226   have identical force-dependent detachment rate profiles ($k_{off}(F)$) at F>2 pN and F<-1 pN

227   as their kinesin-2 peer, KIF3A/B, which has been thoroughly characterized by optical

228   trapping experiments [46]. As no experimental data are available for force-dependent

229   detachment rates at very low forces, exponential interpolations were used to connect

230   detachment rates at -1 pN and +2 pN to the measured zero-load motor off-rate (Figure

231   S7B; see Materials and Methods for further details). Using this approach, simulated

232   single-molecule velocities of FLA8/8 (1954 ± 117 nm/s) and KLP11/20 (587 ± 82 nm/s;

233   N=1000 runs for each), calculated by linear fits to position vs time traces (Figure 3B and

234   Figure S8A), were in good agreement with experimental values (Table S1). The

235   corresponding run length distributions for FLA8/8 (Figure 3C; mean 2.12 ± 0.13 μm) and

236   KLP11/20 (Figure S8B; mean 2.28 ± 0.15 μm) also agreed well with experiments (Table
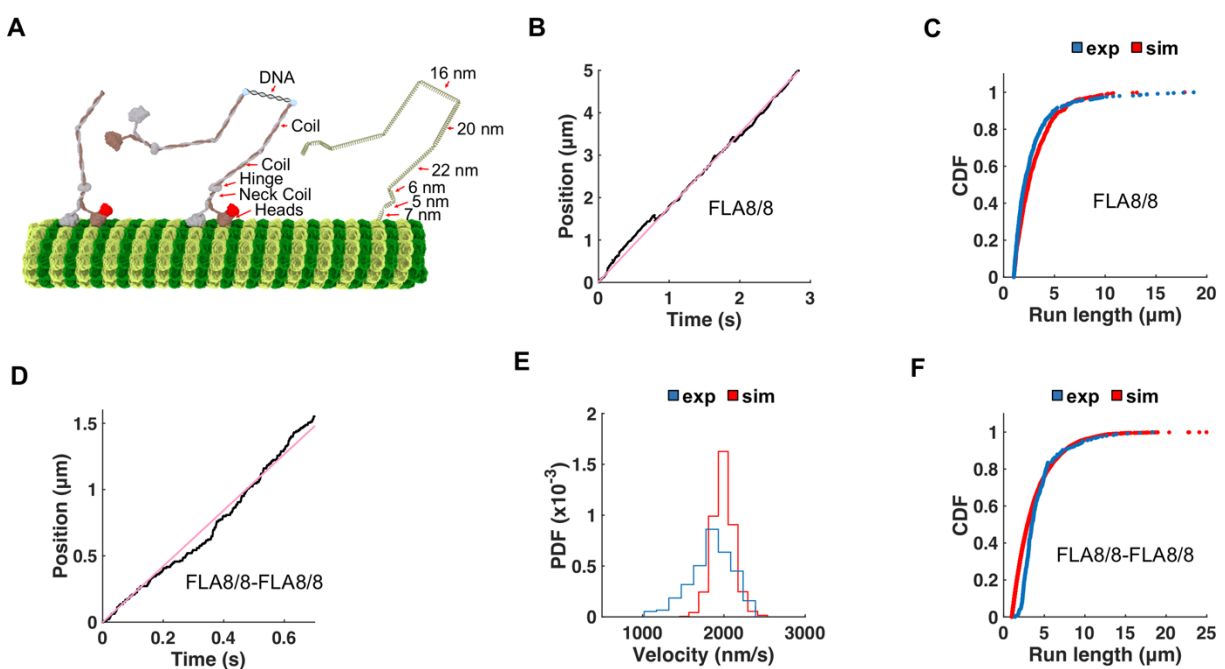
237   S1).

Figure 3: Model recapitulates kinetic parameters of FLA8/8 and FLA8/8-FLA8/8 co-transport. (A) Illustrations of a single kinesin-2 (left), a motor-DNA hybrid construct (middle), and the FJC simulation model (right). The springs shown on the right correspond to the two kinesin-2 motors (head, neck coil, hinge, coil1, coil2), and the dsDNA. **(B)** Positions (black) of a single FLA8/8 motor from the simulations as a function of time (tracked at the head). The simulated velocities were calculated from the slope of each trace (pink line). **(C)** Cumulative distributions of experimental (blue) and simulated (red) run lengths of a single FLA8/8 motor (Table S1). **(D)** Positions (black) of the FLA8/8-FLA8/8 co-transport from the simulations as a function of time (tracked in the middle of the dsDNA). **(E)** Experimental (blue) and simulated (red) velocity distributions of FLA8/8-FLA8/8 co-transport. The means and standard deviations were determined by fitting to a Gaussian function; 1806 ± 339 nm/s (experiment), 1927 ± 124 nm (simulation). The simulated velocity was calculated from the slope of each trace (pink line). **(F)** Cumulative distributions of experimental (blue) and simulated (red) run lengths of FLA8/8-FLA8/8. The mean run lengths determined by fitting the cumulative distribution function (CDF) are 3.00 ± 0.06 μm for the experiment and 2.80 ± 0.11 μm for the simulation, respectively.

Having validated our single-molecule simulations, we next turned to modeling the co-transport behaviors of FLA8/8-FLA8/8 (Figure 4A) and KLP11/20-KLP11/20 (Figure 4B). Simulations were initialized by binding of one motor to the microtubule and allowing the second motor to attach with a reattachment rate (k_{on}) that was the only open parameter in the simulations. Simulations terminated when both motors detached from the microtubule. The motor-DNA hybrid was tracked at the motor domains when only one motor was bound, and at the mid-point between the two motors when both motors were bound. Sample traces of simulated FLA8/8-FLA8/8 and KLP11/20-KLP11/20 co-transport are shown in Figure 3D and Figure S8C respectivaly. Reattachment rates (k_{on}) were

263 varied to find the best match of simulations to the experimental velocities and run lengths

264 of the corresponding motor pairs. The reattachment rates that best recapitulated the

265 experiments were 4 s^{-1} for FLA8/8 and 2.5 s^{-1} for KLP11/20 (Figures 3E and 3F, Figures

266 4C–G, Figures S8D and S8E, Figure S9, Suppl movies 4 and 5). The velocity and run

267 length values are summarized in Table S1, and simulation parameters are given in Table

268 S2.

269

270 Having identified a parameter set that recapitulates the experimental behavior of the

271 motor pairs, we then used the simulations to investigate motor behavior and inter-motor

272 coupling during co-transport. To determine whether different motors are able to better

273 coordinate in groups than others, we calculated the co-transport velocity efficiencies by

274 dividing the average velocity of the motors during co-transport by their respective

275 unloaded velocities. Based on the simulations, the velocity efficiencies of FLA8/8 and

276 KLP11/20 were similar and were both only slightly lower than 1 (Figure. 4H); thus, by this

277 metric their co-transport abilities were similar despite their four-fold different speeds. Next,

278 to investigate the attachment/detachment dynamics during co-transport, we calculated

279 the fraction of time each complex spent with only one motor bound versus both motors

280 bound (Figure 4I). For both FLA8/8-FLA8/8 and KLP11/20-KLP11/20, the complexes

281 spent roughly 80% of the time with only one motor bound and transporting the complex.

282 Thus, in the majority of traces, the second motor could not land before the first motor

283 detached from the microtubule, or one of the motors detached due to the high detachment

284 rates under load during co-transport. This result is consistent with the finding that the run

285 lengths of the FLA8/8-FLA8/8 and KLP11/20-KLP11/20 complexes were only slightly

286 higher than their corresponding single-molecule run lengths (Table S1). To summarize,

287 when working in pairs, both FLA8/8 and KLP11/20 generally work as single-molecules

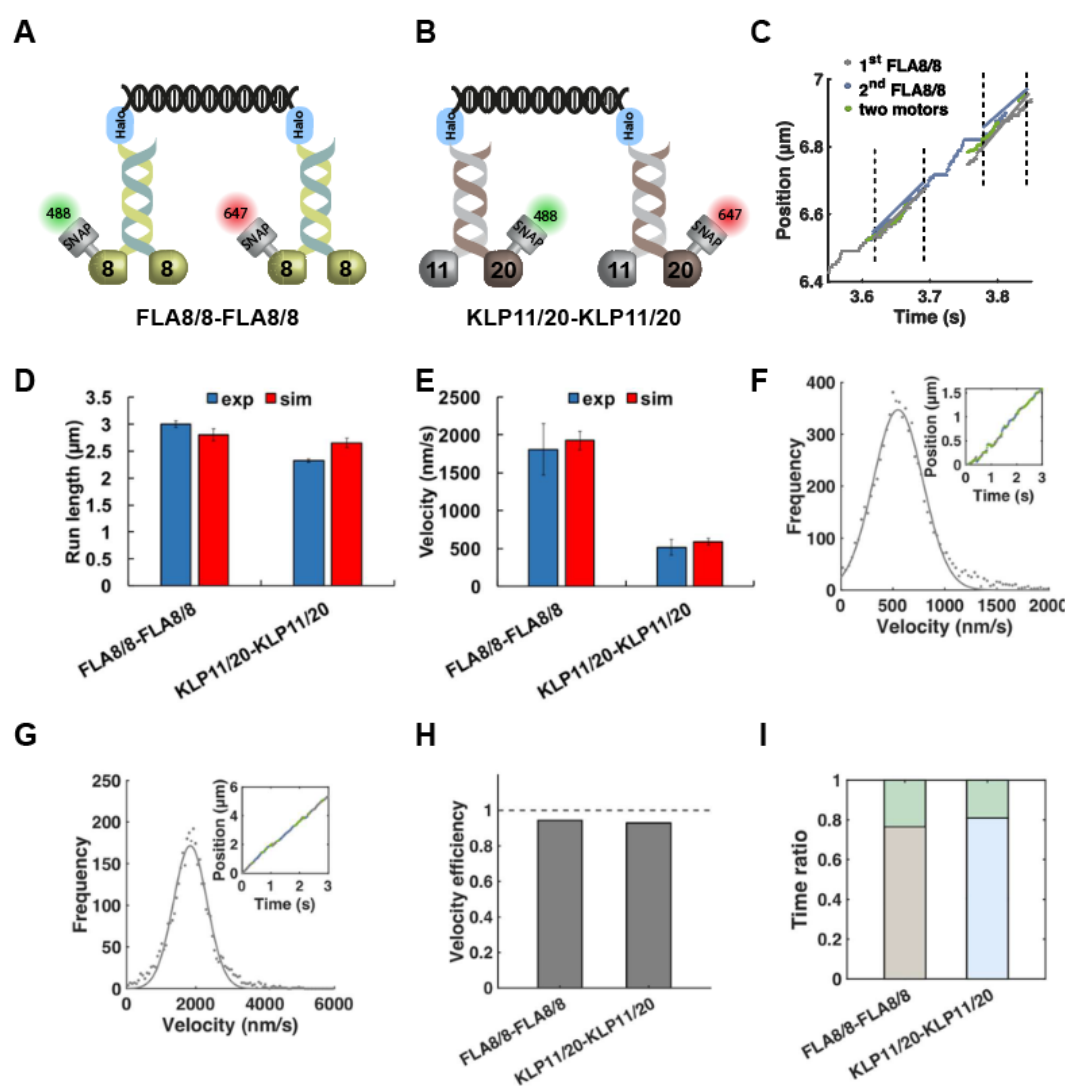288 rather than cooperating with their partner in the complex.

289

Figure 4: Simulations recapitulate experimental results of co-transport by FLA8/8 and KLP11/20 pairs. (**A**) **and** (**B**) depict coupling of two fast and two slow motors, respectively. **(C)** Simulated trace of FLA8/8-FLA8/8 co-transport. Trace shows position of the first motor (grey) or the second motor (blue) when only one motor is bound to the microtubule, or the position of the middle of the complex (green) when both motors are simultaneously bound to the microtubule. The regions bounded by two vertical dashed lines represent periods of co-transport. **(D)** Run length, and **(E)** velocity data comparing experiments (blue) with simulations (red). Error bars indicate mean ± SD. **(F) and (G)** Velocity histogram of KLP11/20 **(F)** and FLA8/8 **(G)** motor-DNA hybrids during their co-transport. Co-transport velocities (grey circles) in simulations were measured by linear fits to the traces during periods when both motors were bound to the microtubule; see (C) for FLA8/8-FLA8/8 co-transport and Figure S9 for KLP11/20-KLP11/20 co-transport. **(H)** Motor velocity efficiencies (co-transport velocity divided by the unloaded velocity of single motors) during co-transport for FLA8/8-FLA8/8 (0.94 efficiency) and KLP11/20-KLP11/20 (0.93 efficiency). **(I)** Fraction of time simulated motor-DNA hybrids spent in one- or two-motor bound states. Of total transport time, FLA8/8-FLA8/8 spent 0.76 with one motor bound (gray), and KLP11/20-KLP11/20 spent 0.81 of time with one motor bound (blue).

305

Collectively, our *in vitro* and *in silico* dissections provide key mechanistic insights into IFT in the flagella of *C. reinhardtii* where IFT by kinesin-2 was first identified [13]. We demonstrate that heterotrimerization with the KAP subunit, as occurs *in vivo*, relieves

309   auto-inhibition in the heterodimeric FLA8/10 kinesin-2 and fully activates the motor for

310   efficient and atypically fast processive transport *in vitro*. The heterotrimeric FLA8/10/KAP

311   transport complex is thus necessary and sufficient for the previously observed

312   anterograde IFT in *C. reinhardtii*. We pinpoint this so far unique kinetic property to the

313   catalytic heads of the heterodimeric FLA8/10. However, irrespective of species-specific

314   kinetics, the kinesin-2 motors from the unicellular *C. reinhardtii* and multicellular *C.*

315   *elegans* both display similar uncooperative behavior during co-transport suggesting that

316   these motors share common principles to accomplish efficient IFT *in vivo*.

317

Acknowledgments

325

Author contributions

327   P.S. and Z.Ö. designed the experiments. P.S. and A.C. performed experiments and

328   analyzed the data. W.L.S. wrote all customized MATLAB routines. W.Y. developed the

329   model, performed the simulations, analyzed data, prepared the figures; P.W. analyzed

330   data, prepared figures; I.S.M. developed the Monte Carlo simulations for calculating the

331   landing distributions; E.T. supervised all the modeling work. Z.Ö., P. S., W. O. H, W.Y.,

332   P.W. and E.T. contributed to the manuscript writing.

333

Competing financial interests

335   The authors declare no competing financial interests.

336

Supporting information

SI Materials and Methods

All reagents were the highest purity available and were obtained from Sigma-Aldrich unless stated otherwise.

Protein expression, purification and fluorescent labeling

Proteins were expressed using the Baculovirus Expression System in insect cells (Spodoptera frugiperda, Sf9) according to the manufacturer's instructions (Life Science Technologies). Proteins were Flag-tagged (DYKDDDDK) at their C- or N-terminal ends to facilitate purification. Cells (protocol for 50 ml culture) were harvested by centrifugation @1500 rpm for 15 minutes. Purification was performed at 4 °C. Cell pellets were lysed in lysis buffer (10% Glycerol, 50 mM Pipes, pH 6.9, 300 mM potassium acetate (KAc), 1 mM $MgCl_2$, 1 mM DTT, 0.1 mM ATP, 0.5% Triton X-100, complete protease inhibitor tablet (Roche)). Cell debris were removed by centrifugation at 30000 rpm for 10 minutes at 4 °C. Supernatant was incubated with 100 µl of Anti-Flag M2 affinity gel at 4 °C for 90 minutes. Beads were centrifuged at 800 rpm for 15 minutes at 4 °C and washed three times with 1 ml of wash buffer 1 (10% Glycerol, 80 mM Pipes, pH 6.9, 500 mM KAc, 1 mM $MgCl_2$, 1 mM DTT, 0.1 mM ATP, 0.1% Tween-20, complete EDTA-free protease inhibitor cocktail (Roche)) and three times with 1 ml of wash buffer 2 (10% Glycerol, 80 mM Pipes, pH 6.9, 200 mM KAc, 1 mM $MgCl_2$, 1 mM EGTA, 1 mM DTT, 0.1 mM ATP, 0.1% Tween-20, complete EDTA-free protease inhibitor cocktail (Roche)). For fluorescent labeling, beads were incubated for 45 minutes on a rotator at room temperature with wash buffer 2, containing 10 µM SNAP-Surface Alexa Fluor[488] or SNAP-surface Alexa Fluor[647] (New England Biolabs). Excess dye was removed by washing the beads three times with 1 ml of wash buffer 2, and labeled protein was eluted in elution buffer (Wash buffer 2 containing 0.5 mg/ml 1X Flag peptide) after 45 minutes of incubation at 4 °C. Purified proteins were analyzed by SDS-PAGE on a 10% polyacrylamide gel. Multi-motor gliding assays were performed as described previously to ensure motor protein quality [29].

Proteins used in this study

1. FLA8[C-Flag]/FLA10[C-His]

2. FLA8[C-Flag]/ [N-SNAP]FLA10[C-His]

3. [N-SNAP]FLA8 [C-Halo-Flag]/FLA8[(10 stalk) C-His]

4. FLA10$^{(8\ stalk)\ C\text{-}Flag}$/FLA10$^{C\text{-}His}$

5. KLP11$^{C\text{-}Halo\text{-}His}$/$^{N\text{-}SNAP\text{-}Flag}$KLP20 (with activating mutations as described in [29])

6. FLA8$^{(KLP20\ stalk)\ C\text{-}Flag}$/$^{N\text{-}SNAP}$FLA10$^{(KLP11\ stalk)\ C\text{-}His}$

Splice sites used in this study are indicated below [29].
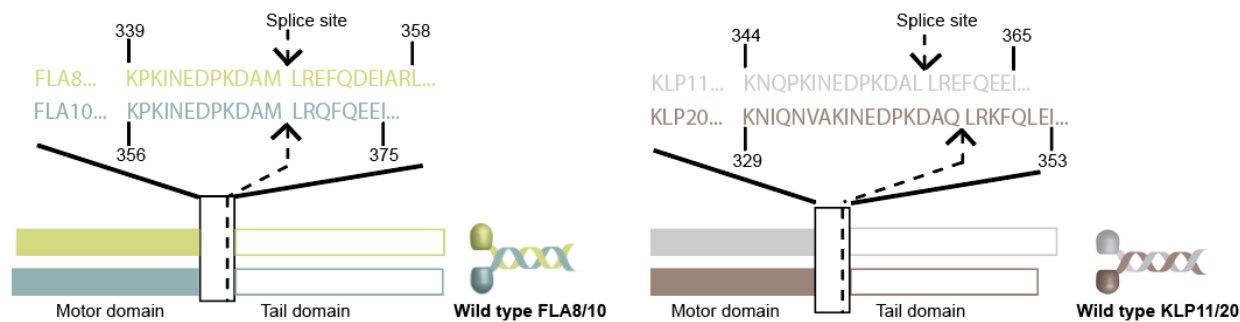
Assembly of the Motor-DNA hybrids

I. **Covalent coupling of one motor to dsDNA**

For specific coupling of motor to DNA, double-stranded DNA (dsDNA) was synthesized with Atto-633 dye on one strand and with a thiol group on the complementary strand (Biomers):

5'-ATTO633-CCG AGG ACT GTC CTC CCG AGT GCG GCT ACG ACG TTA CCC GGG TGA GCA-3'

5'-TGC TCA CCC GGG TAA CGT CGT AGC CGC ACT CGG GAG GAC AGT CCT CCG-Thiol C6-3'

Purification and activation of fluorescent thiol-dsDNA:

The single-stranded DNA oligonucleotides containing the fluorescent dye and the thiol-group were mixed in an equimolar concentration and incubated for 30 minutes at room temperature. The sulfhydryl-groups (-SH) were regenerated by the addition of 1/10 volume of TCEP and the mixture was incubated for 30 minutes at room temperature. The DNA solution was mixed with of 1/10 volume of sodium acetate (NaAc) and subsequently with 2.5× volume of ice-cold ethanol and incubated for 1 hour at -20°C and centrifuged for efficient precipitation. The DNA pellet was centrifuged at 14000 rpm for 30 minutes at 4°C and washed with 70% ethanol. The pellet was resolubilized in ammonium bicarbonate buffer (containing 1mM TCEP) and immediately reacted with five-fold excess of the Halo Iodoacetamide O4 ligand and incubated for 45 minutes on a rotator at room temperature. Unreacted Iodoacetamide ligand was removed via HPLC and the functionalized DNA was stored at -20°C for long term use. The C-terminally Halo-tagged and fluorescently labeled motors (Figure S3) were covalently linked to the Iodoacetamide-

396   functionalized dsDNA [47, 48] by simply mixing in a 1:1 ratio (for coupling specificity and

397   efficiency see Figures S4 and S5).

398   **Buffers and solutions:**

399   TECP: 100 mM in ddH$_2$0

400   NaAc: 3 M in ddH$_2$0, pH 5.2

401   Ammonium bicarbonate: 200 mM, pH 8.0

402   Halo Iodoacetamide O4 ligand (Promega): 100 mM in DMSO

403   Wash buffer: 80 mM Pipes, pH 6.9, 200 mM KAc, 1 mM MgCl$_2$, 1 mM EGTA, 1 mM DTT,

404   0.1% Tween-20, complete EDTA-free protease inhibitor cocktail.

405   **II. Covalent coupling of two motors to dsDNA**

406   To specifically couple two motors to dsDNA, same strategy as above has been followed

407   except, in this case dsDNA is unlabeled and one strand of dsDNA is functionalized with

408   two thiol groups that in turn was covalently linked to the Halo Iodoacetamide O4 ligand

409   (Biomers):

410   5'-CCG AGG ACT GTC CTC CCG AGT GCG GCT ACG ACG TTA CCC GGG TGA GCA-3'

411   5'-Thiol C6-TGC TCA CCC GGG TAA CGT CGT AGC CGC ACT CGG GAG GAC AGT CCT CCG-Thiol

412   C6-3'

413   To couple two differently labeled motors (SNAP[488] and SNAP[647]), the bi-functionalized

414   unlabeled dsDNA was incubated with both motors in equimolar concentrations for 20

415   minutes at room temperature (for coupling specificity and efficiency see Figures S4 and

416   S5).

417

418   **Buffers for TIRF assays:**

419   BRB10: 10 mM Pipes, pH 6.9, 1 mM EGTA, 2 mM MgCl$_2$, 5 mM DTT.

420   BRB10/BSA wash buffer: BRB10 plus 2 mg/ml Bovine Serum Albumin (BSA).

421   BRB10 motility buffer: BRB10 plus 0.145 mg ml^{-1} glucose oxidase,

422   0.0485 mg ml^{-1} catalase, and 20% glucose.

423

424   **Single-molecule and colocalization assays:**

425   Single-molecule and colocalization assays were performed as previously described [31,

426   39]. Briefly, biotinylated microtubules were attached to the glass surface of the flow

427   chamber that was pre-coated with biotinylated BSA and Streptavidin (each 1 mg ml^{-1}).

428   Fluorescent motors were diluted in BRB10 supplemented with 8 mM ATP,

429   0.18 mg ml^{-1} glucose oxidase, 0.06 mg ml^{-1} catalase, and 0.4% glucose. Diluted

430   proteins were incubated with surface-attached microtubules for 2 minutes in the flow

431   chamber and washed with BRB10 buffer supplemented with 2mg/ml BSA. Images of

432   single motors walking on filaments were recorded with a cycle time of 76 ms with an

433   objective-type Leica DMI6000 B TIRF microscope (Leica), equipped with an oil-

434   immersion 100× Plan objective lens (numerical aperture 1.47), and a back-illuminated

435   Andor U897 EMCCD camera (Andor). Excitation was achieved by diode lasers at 488

436   or 638 nm wavelength, and frames were recorded and analyzed with the AF 6000

437   software (Leica). Velocities and run lengths were analyzed with custom-written

438   programs implemented in MATLAB (MathWorks, Natick, MA). Runs (distance from start

439   position to the position with the largest distance) with minimum 1 μm were considered

440   as processive (χ_0 = 1 μm). Histograms of velocities were fitted to a Gaussian distribution,

441   and run-lengths were fitted by a single-exponential model to the empirical Cumulative

442   Distribution Function (CDF) of the measured runs. Runs were included only if they moved

443   smoothly for at least 5 frames and had r^2 value > 95%.

444   For colocalization assays, the same procedure was followed except two channels (488

445   nm and 638 nm) were used for simultaneous observation of both motors. The cycle

446   time for both channels was 195 ms. Colocalized movies were analyzed using custom-

447   written routines in MATLAB (MathWorks, Natick, MA). In order to assign colocalized

448   runs, a penalty score was calculated for all combinations of two runs from the

449   respective channels. The penalty score resulted from the mean distances of tracked

450   positions (pixels, factor 1/3) and the difference in the starting time (frames, factor 1).

451   Long runs were cropped to the length of the shorter runs in order to account for

452   bleaching events. Pairs of runs with a penalty score <10 were considered colocalized

453   and their parameters were taken into account in further analysis as the average values

454   of both runs.

455

456

457

458

459 **Microtubule decoration assays**

460 To determine the coupling efficiency of motor-DNA hybrids, decoration assays were

461 performed by preparing the following mixtures and incubating for 20 minutes at room

462 temperature:

463 **A.** Labeled motor ([N-SNAP488]FLA8/8 or KLP11/ [N-SNAP488]20) without C-terminal Halo-tag was

464 mixed in equimolar concentration with Atto-633 dsDNA functionalized at one end with

465 thiol plus Halo Iodoacetamide O4 ligand.

466 **B.** Labeled motor ([N-SNAP488]FLA8[C-Halo]/8 or KLP11[C-Halo]/ [N-SNAP488]20) was mixed in equimolar

467 concentration with Atto-633 dsDNA functionalized at one end with thiol minus Halo

468 Iodoacetamide O4 ligand.

469 **C.** Labeled motor ([N-SNAP488]FLA8[C-Halo]/8 or KLP11[C-Halo]/ [N-SNAP488]20) was mixed in equimolar

470 concentration with Atto-633 dsDNA functionalized at one end with thiol plus Halo

471 Iodoacetamide O4 ligand.

472 **D.** Differently labeled motors ([N-SNAP488]FLA8[C-Halo]/8, [N-SNAP647]FLA8[C-Halo]/8 or KLP11[C-Halo/N-

473 [SNAP488]20, KLP11[C-Halo/N-SNAP647]20) were mixed in equimolar concentration with unlabeled

474 dsDNA functionalized at both ends with thiols plus Halo Iodoacetamide O4 ligand.

475 Unlabeled microtubules were attached to the glass surface of the flow chamber coated

476 with a Biotinyted BSA-Streptavidin (1 mg ml^{-1} each) sandwich. Mixture (A/B/C/D) was

477 diluted to the desired concentration in BRB10 motility buffer and flowed into the chamber.

478 Images were captured at different locations of the surface. Colocalization efficiencies

479 were analyzed using a custom-written MATLAB routine (MathWorks, Natick, MA).

480

481 **Computational Model:** The model for the motor-DNA hybrid transport is an extension of

482 our earlier work on kinesin-1 and -3 motors [49]. However, instead of explicit Brownian

483 dynamics of the motors attached to a scaffold, it employs a freely jointed chain (FJC)

484 model for the entire kinesin-scaffold-kinesin construct. The whole construct is modeled in

485 three dimensions, and consists of 11 rigid segments of non-uniform-lengths, as illustrated

486 in Figure 3A. The microtubule (MT) is modeled as a 25 nm diameter cylinder anchored

487 on glass surface with the scaffold-motor complex placed on top.

488 We developed a separate Monte-Carlo simulation to calculate the distribution of

489 the end-to-end distance of the motor-DNA hybrid, *P(R),* and its standard deviation, *σ,*

490   which is used to determine attachment locations in the 3D geometry (Figure 3A). In this

491   model, a point is first placed on the microtubule, and a second point is generated using

492   random values with uniform distributions between $[0,\pi)$ and $[0, 2\pi)$ for the two

493   corresponding spherical angles, θ and ϕ, respectively. We then continued this procedure

494   to grow the scaffold, one segment at a time, with the segment lengths shown in Figure

495   3A. Any configuration that intersects the cylindrical microtubule at any location is rejected,

496   and the accepted configurations are projected along the backbone of the microtubule. We

497   then calculated a histogram (Figure S6A), and fit it to a Gaussian to calculate the standard

498   deviation, σ, of end of end distances, i.e. the landing distance distribution.

499   During co-transport, both motors are subject to forces of the same magnitude but

500   in opposite directions. The front motor (toward the plus end) is under a hindering load

501   (negative), whereas the rear motor (toward the minus end) is under an assisting load

502   (positive). The force-extension curve is modeled in a piece-wise manner, as shown in

503   Figure S6B, namely

504
$$F(x) = \begin{cases} 0.06x, & \text{low force} \\ 0.32 \cdot \dfrac{1}{1-\frac{x}{136}}, & \text{high force} \end{cases} \tag{1}$$

505   where x is the end-to-end distance (nm), F is the force acting on the motor (pN), and 136

506   nm corresponds to the total contour length of the complex.

507   At each time step, motors stochastically take a step of 8 nm based on a probability

508   of stepping given by

509
$$p_{step} = 1 - e^{-v\tau/\delta} \tag{2}$$

510   where v is the motor velocity, τ is the simulation time step, and δ is the step size. The

511   linear force-velocity curve was taken from [50] as follows (see also Figure S7A)

512

513
$$v(F) = \begin{cases} 0, & F < F_{stall} \\ v_u \left(2 - \dfrac{2F}{F_{stall}}\right), & F < 0 \\ v_u, & F \geq 0 \, , \end{cases} \tag{3}$$

514   Where v_u is the unloaded velocity, F is the force acting on the motor and F_{stall} is the stall

515   force (6 pN) [29].

516   Motors stochastically dissociate from the MT based on the force-dependent

517   detachment rate, $k_{off}(F)$, of kinesin-2, previously measured by Milic et al. [46]. Due to the

518   lack of experimental data at low forces (-1 to 2 pN), we utilized exponential interpolations

519 towards the known $k_{\text{off},0}$ value, resulting in the force-dependent detachment rate given by

520
$$
k_{\text{off}}(F) = \begin{cases} 9.714e^{-0.177F} - 7.678, & F < -1 \\ k_{\text{off}}(0)e^{-\ln\left(\frac{3.919}{k_{\text{off}}(0)}\right)F}, & -1 \leq F < 0 \\ k_{\text{off}}(0)e^{\ln\left(\frac{8.168}{k_{\text{off}}(0)}\right)F}, & 0 \leq F < 2 \\ 6.505e^{0.114F}, & F \geq 2 \end{cases}
\tag{4}
$$

521 where $k_{\text{off}}(0)$ represents the unloaded detachment rate (= velocity/run length) (plotted in

522 Figure S7B). After a motor detaches from the MT, it diffuses within a range of the contour

523 length (136 nm) and can reattach back to the MT based on the reattachment rate, k_{on}.

524

525 **Data availability**

526 All raw data sets used for the analysis or (full pictures of decoration images or colocalised

527 movies) and MATLAB codes are available from the corresponding author on request.
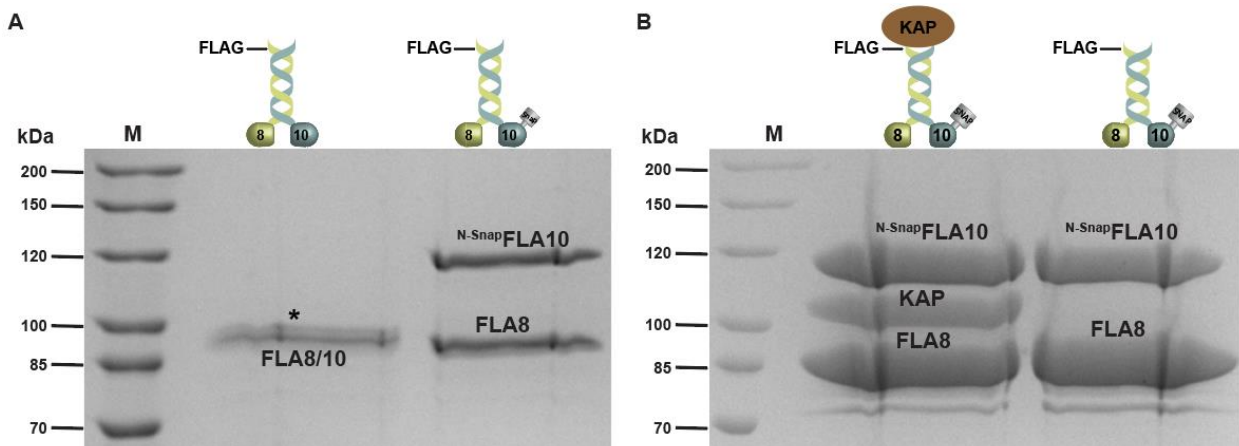
528

529

Supplementary Figures

Figure S1: (A) FLA8 and FLA10 subunits form a heterodimeric kinesin-2 motor. SDS-PAGE analysis of the heterodimeric full-length FLA8/10 motor after FLAG-affinity-Tag purification of the C-terminally Flag-tagged FLA8 and the C-terminally 6X-His-tagged FLA10 subunits. **M**: marker. The C-terminally Flag-tagged FLA8 co-precipitates the 6X-His-tagged FLA10. The identity of the protein bands cannot be distinguished due to their similar sizes (~87 kDa) (first lane after marker). The FLA10 subunit was N-terminally SNAP-tagged to distinguish the respective subunits. The C-terminally Flag-tagged FLA8 efficiently co-precipitated the 6X-His-tagged FLA10 subunit demonstrating the heterodimerization of the FLA8 and FLA10 subunits (second lane after marker). **(B) FLA8, FLA10 and KAP form a heterotrimeric kinesin-2 motor.** SDS-PAGE analysis of the full-length heterotrimeric FLA8/10/KAP (first lane after marker) and heterodimeric FLA8/10 (second lane after marker) kinesin-2 complexes after FLAG-affinity-Tag purification via the C-terminally Flag-tagged FLA8 subunit.
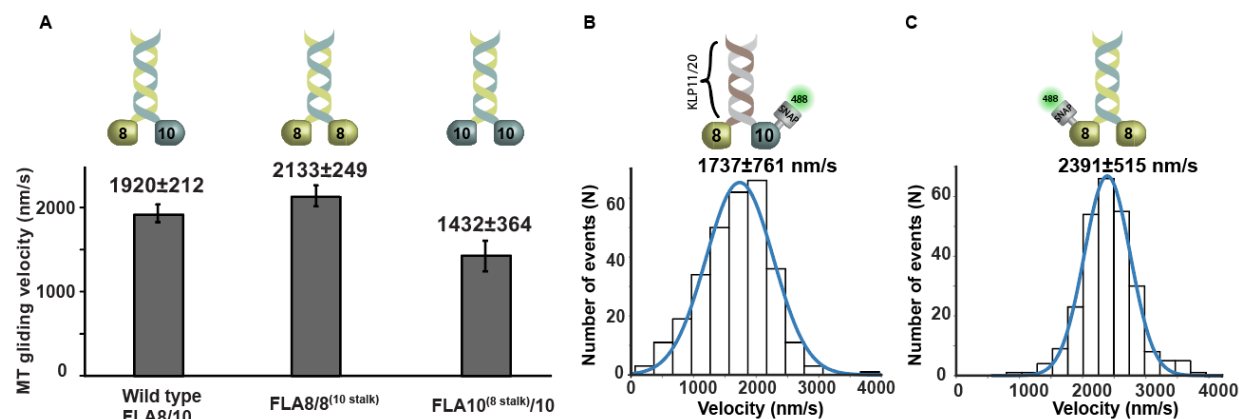

Figure S2: (A) The heterodimeric FLA8/10 kinesin-2 motor combines a fast FLA8 and a slow FLA10 head domain. Multiple-motor filament gliding assay of surface-attached motors moving fluorescently labeled microtubules (Suppl. movie 1). The wild type FLA8/10 (left) displays fast filament gliding velocities (1920±212 nm/s, N=30), as surface-binding via the stalk/tail abolishes the auto-inhibition (compare to the single-molecule behavior in Figure 2A). The chimeric FLA8/8 (middle) moves microtubules faster (2133±249 nm/s, N=30) than wild-type, whereas the FLA10/10 chimera (right) moves microtubules slower (1432±364 nm/s, N=30) than wild-type. Schematic (middle top) depicts the chimeric FLA8/8(10 stalk) motor that was constructed by replacing the FLA10 head domain with the FLA8 head; similar strategy used for FLA10/10(8 stalk) (right top). **(B) Catalytic heads as the main determinants of the kinesin-2-driven IFT**

553   **velocity in *C. reinhardtii*.** Schematic showing replacement of the head domains in the wild type KLP11/20

554   heterodimer with the FLA10 and FLA8 head domains creates a chimeric motor, FLA8[(KLP20)]/FLA10[(KLP11)]

555   with substantially increased velocity 1737±761 nm/s (N=296). **(C) Fast and fully active FLA8/8[(10 stalk)]**

556   **motor.** Single FLA8/8[(10 stalk)] motors were tracked via the fluorescently labeled SNAP- tag on the N-terminus

557   of the FLA8 subunit. Removal of the FLA10 head domain abolished the slow velocity distribution (Figure

558   2A, v1) and in the FLA8/8 chimera displayed a fast velocity of 2391±515 nm/s (N=262) similar to the fast

559   v2 of the wild type FLA8/10 (Fig. 2A). Error bars indicate mean ± s.d. Data is fitted to a Gaussian

560   distribution (±width of distribution, from two independent experiments).
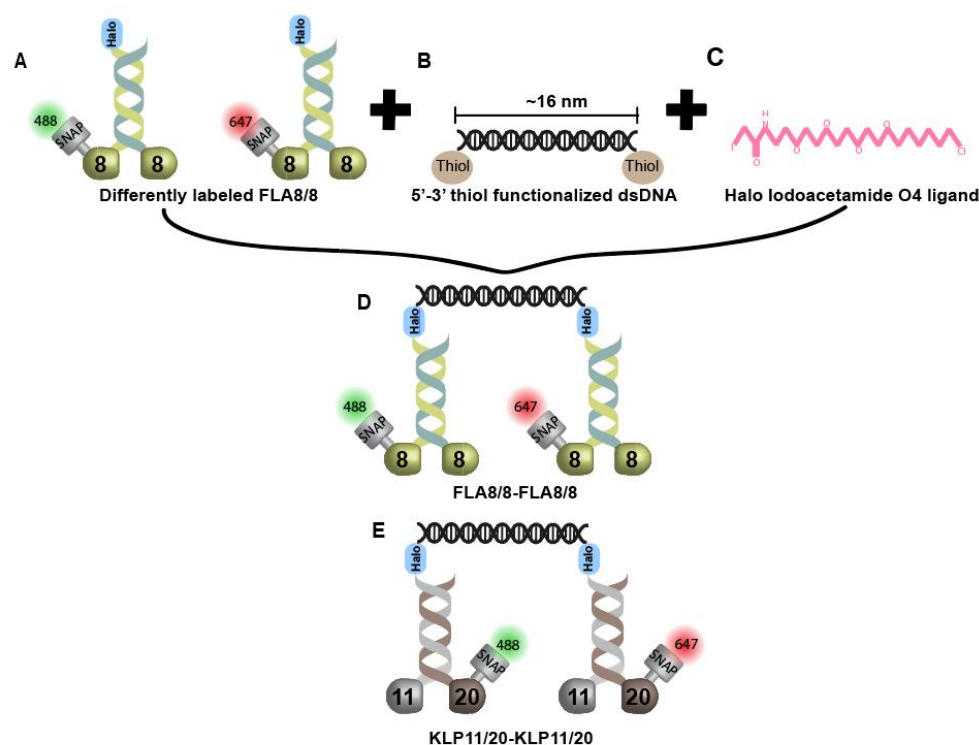
561

562

563   **Figure S3: Coupling of two kinesin-2 motors with exclusive specificity. (A)** The C- terminal Halo-tag

564   was used to couple the Iodoacetamide-functionalized dsDNA to the differentially labeled FLA8/8 chimeras

565   (SNAP[488] and SNAP[647] dyes). **(B)** dsDNA (48bp) was bi-functionalized with two thiol groups at both ends.

566   **(C)** The Halo Iodoacetamide O4 ligand was coupled to the thiol-functionalized dsDNA. **(D)** Two FLA8/8

567   motors labeled with different fluorophores, [SNAP488]FLA8[C-Halo]/8[(10 stalk)] and [SNAP647]FLA8[C-Halo]/8[(10 stalk)], were

568   mixed in equimolar concentrations with the Iodoacetamide-bi-functionalized dsDNA to assemble a stable,

569   covalently linked motor-DNA hybrid. **(E)** depicts coupling of two slow motors KLP11[C-Halo/] [SNAP488]20 and
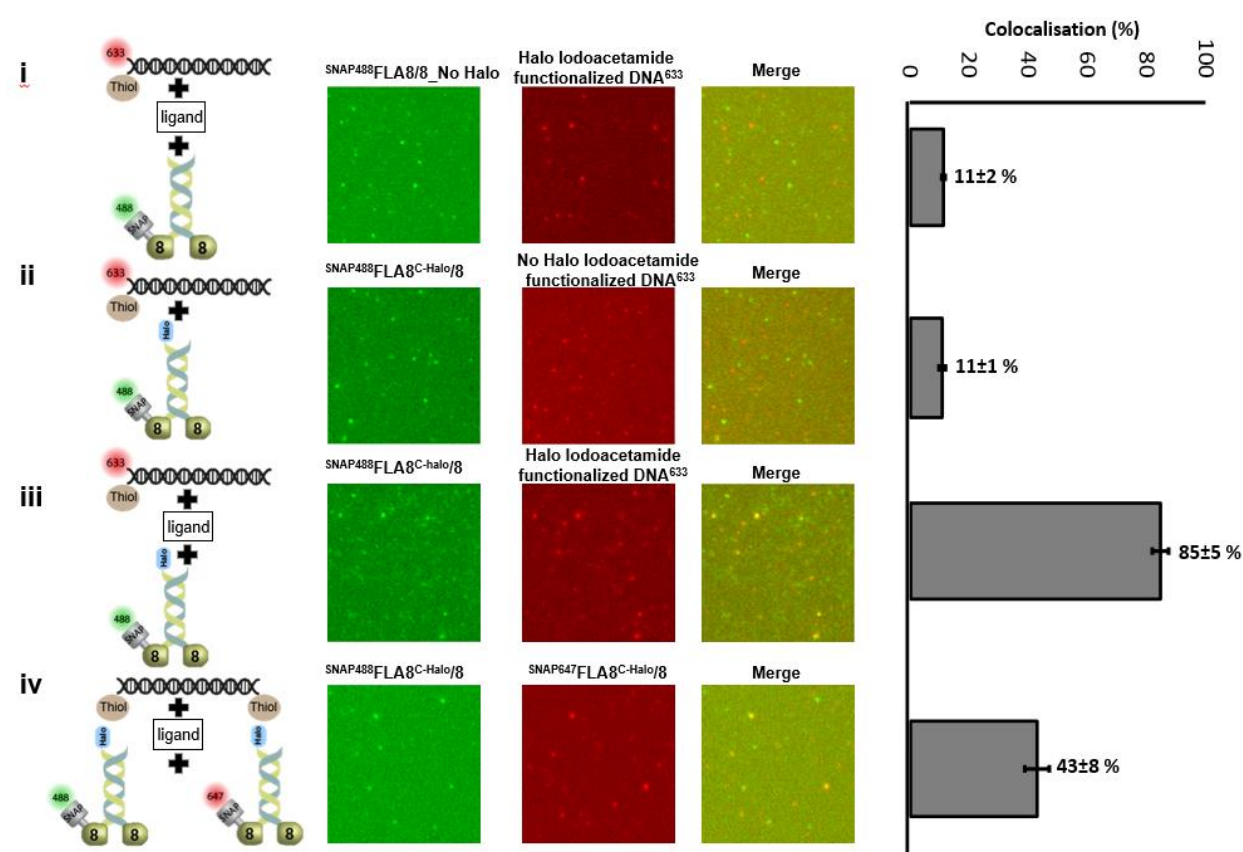
570   KLP11[C-Halo/SNAP647]20.

571

Figure S4: Highly specific DNA coupling and labeling of FLA8/8 motors. **i)** SNAP[488]-labeled FLA8/8 (green channel) motor that lacked the C-terminal Halo-tag was mixed in equimolar concentrations with the Atto-633-labeled and Iodoacetamide-functionalized dsDNA (red channel). Quantification on the right shows the corresponding colocalization efficiency of DNA-motor coupling *in the absence of the C-terminal Halo-tag* on the motor. **ii)** SNAP[488]-labeled and C-terminally Halo-tagged FLA8/8 motor was mixed in equimolar concentrations with the Atto-633-labeled and thiol-functionalized dsDNA that lacked the Iodoacetamide ligand (red channel). Quantification on the right shows the colocalization efficiency of DNA-motor coupling *in the absence of the Iodoacetamide ligand* on the dsDNA. **iii)** The presence of both the C-terminal Halo-tag on the FLA8/8 motor and the Iodoacetamide-functionalized dsDNA lead to robust colocalisation (85±5%). **iv)** SNAP[488]-labeled and C-terminally Halo-tagged FLA8/8 was (green channel) was mixed in equimolar concentrations with the SNAP[647]-labeled and C-terminally Halo-tagged FLA8/8 (red channel). The differently labeled motors were in turn mixed in equimolar concentrations with the Iodoacetamide-bi-functionalized (unlabeled) dsDNA. Quantification shows the 43±8% colocalisation efficiency, which is close to the statistically expected 50%. Numbers are mean±s.d.
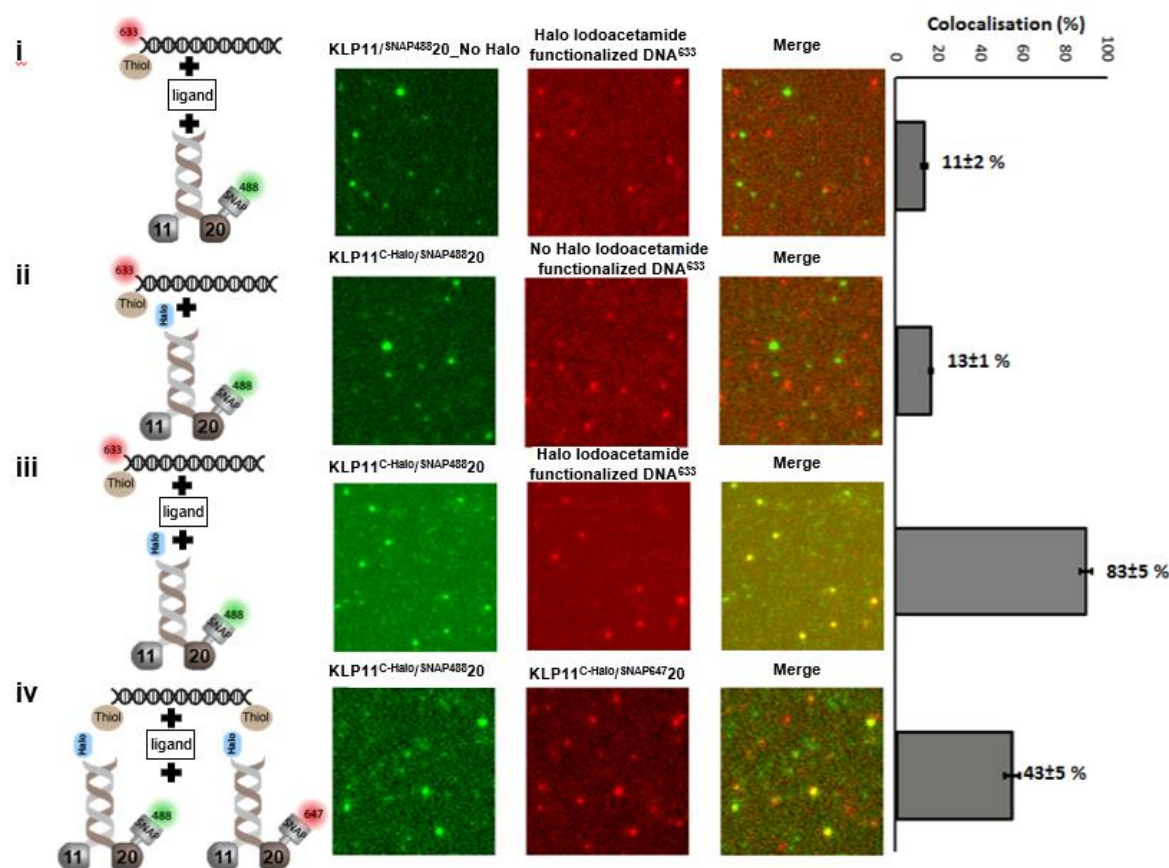
Figure S5: Highly specific DNA coupling and labeling of KLP11/20 motors. **i)** SNAP[488]-labeled KLP11/20 (green channel) motor that lacked the C-terminal Halo-tag was mixed in equimolar concentrations with the Atto-633-labeled and Iodoacetamide-functionalized dsDNA (red channel). Quantification on the right shows the corresponding colocalization efficiency of DNA-motor coupling *in the absence of the C-terminal Halo-tag* on the motor. **ii)** SNAP[488]-labeled and C-terminally Halo-tagged KLP11/20 motor was mixed in equimolar concentrations with the Atto-633-labeled and thiol-functionalized dsDNA that lacked the Iodoacetamide ligand (red channel). Quantification on the right shows the corresponding colocalization efficiency of the DNA-motor coupling *in the absence of the Iodoacetamide ligand* on the dsDNA. **iii)** The presence of both the C-terminal Halo-tag on the KLP11/20 motor and the Iodoacetamide-functionalized dsDNA lead to robust colocalisation (83±5%). **iv)** SNAP[488]-labeled and C-terminally Halo-tagged KLP11/20 (green channel) was mixed in equimolar concentrations with the SNAP[647]-labeled and C-terminally Halo-tagged KLP11/20 (red channel). The differently labeled motors were in turn mixed in equimolar concentrations with the Iodoacetamide-bi-functionalized (unlabeled) dsDNA. Quantification shows the 43±5% colocalisation efficiency, which is close to the statistically expected 50%. Numbers are mean±s.d.
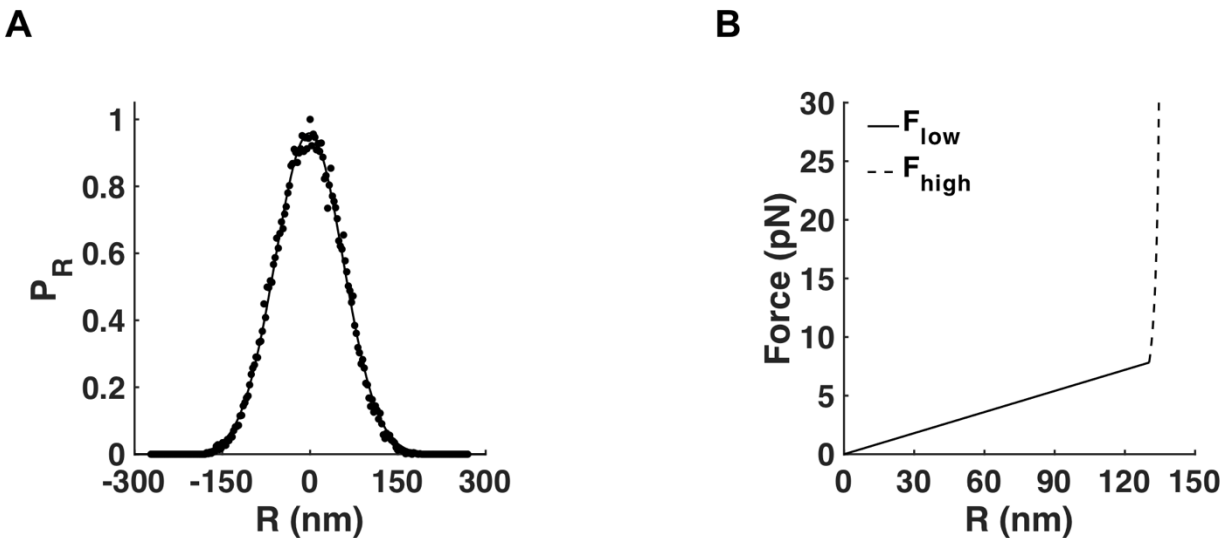
A

B

Figure S6: End-to-end distance distribution and force-extension curve used in the simulations. (A) Probability distribution of end-to-end distance of three-dimensional FJC model with a scaffold length of *136 nm*. The standard deviation of the distribution is *57.35 nm.* **(B)** The force-extension curve used in the simulations: at small forces, ($F \ll kT/\ell$; solid line), Hooke's law is obeyed; at higher forces, ($F \gg kT/\ell$; dashed line), forces increase exponentially with length (see Eq. (1)).

A

B
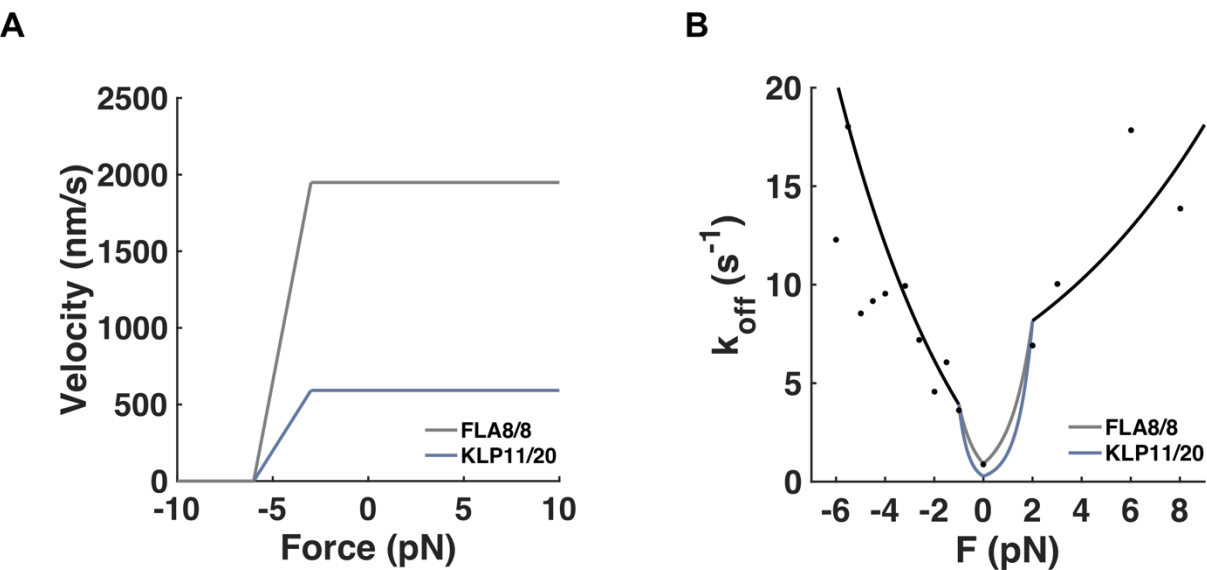
Figure S7: Model parameters. (A) Force-velocity curve of FLA8/8 (grey) and KLP11/20 (blue) used in the simulations. The force-velocity curve of KLP11/20 was estimated from [50]. The force-velocity curve of FLA8/8 was assumed to behave in the same manner as KLP11/20, but the unloaded velocity was adjusted from *592 nm/s* to *1949 nm/s.* **(B)** Force-dependent off-rates of FLA8/8 and KLP11/20 used in the simulations. Black circles show off-rate data measured experimentally by Milic et al. [46]. In our simulations, the off-rates of both FLA8/8 and KLP11/20 in the high-force regime were taken from exponential fits to the data points (black lines). The off-rates from exponential interpolations at low forces are shown for FLA8/8 (grey lines) and KLP11/20 (blue lines). The positive and negative forces refer to the assisting and hindering directions, respectively.

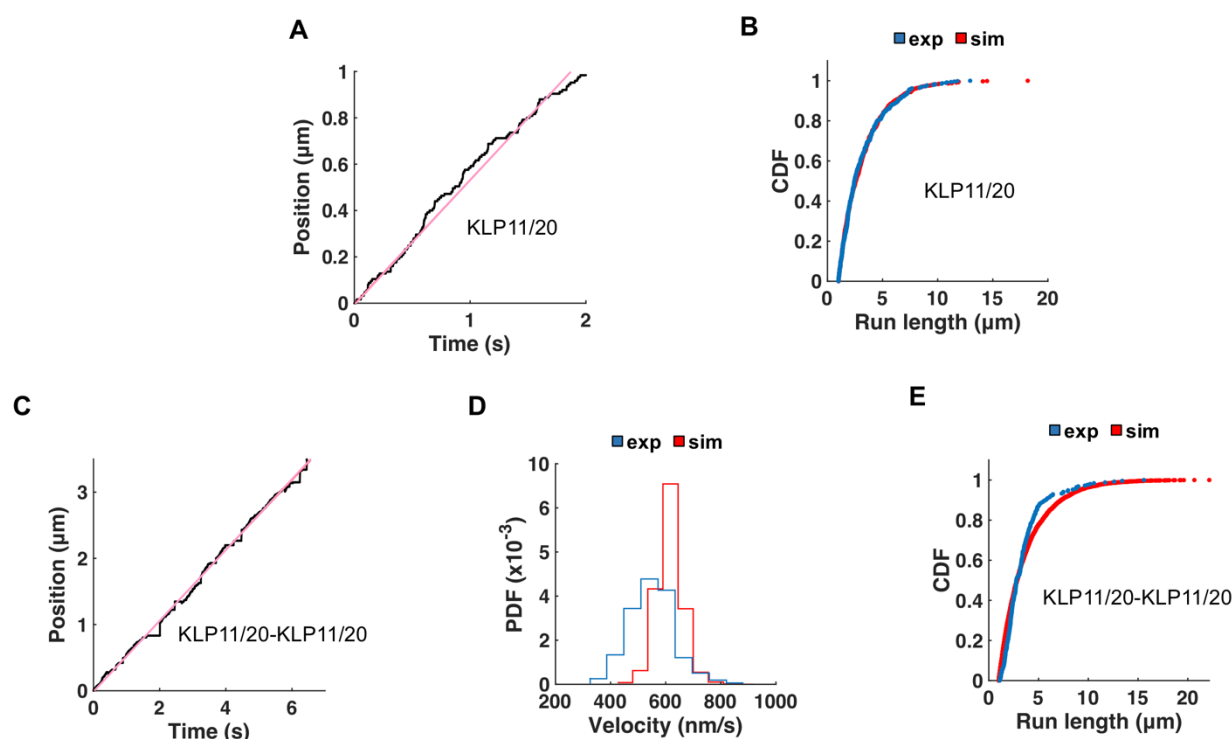**Figure S8: Velocities and run lengths of single KLP11/20 motor and KLP11/20-KLP11/20 co-transport. (A)** Time-dependent positions (black) of single KLP11/20 motor from the simulations. Positions were traced at the motor heads for the single motor simulations. Mean velocity was calculated from the slope of each trace (red lines); values given in Table S1. **(B)** Cumulative distributions of experimental (*blue*) and simulated (*red*) run lengths of single KLP11/20 (Table S1). **(C)** Time-dependent positions (black) of KLP11/20-KLP11/20 co-transport from the simulations. The positions of the complexes were traced in the middle of the dsDNA. **(D)** Velocity distributions of KLP11/20-KLP11/20 from the experiment (blue) and simulation (red). The means and standard deviations were determined by fitting to a Gaussian function, resulting 513 ± 101 nm/s for the experiment and 586 ± 44 nm/s for the simulations, respectively. Simulated velocities were calculated from the slope of each trace (red lines in (C)). **(E)** The mean run lengths of KLP11/20-KLP11/20 co-transport were determined by fitting a CDF, resulting in 2.32 ± 0.03 µm for the experiment and 2.65 ± 0.09 µm for the simulation, respectively.
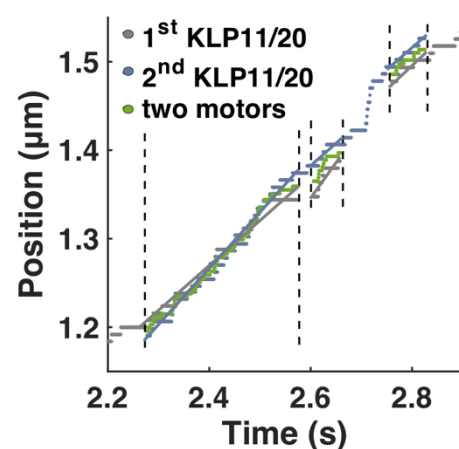

Figure S9: Simulated trace of KLP11/20-KLP11/20 co-transport. Traces show position of the first motor (grey) or the second motor (blue) when only one motor is bound to the microtubule, or the position of the middle of the complex (green) when both motors are simultaneously bound to the microtubule. The regions

639   bounded by two vertical dashed lines represent periods of co-transport. The velocity shown in Figure 4F

640   was calculated from the linear fits (as shown by the straight lines) to the trace during periods of co-transport.

641

642   **Supplementary Tables:**

		FLA	FLA8/8-FLA8/8	KLP	KLP11/20-KLP11/20
Velocity (nm/s)	Exp	1949 ± 408	1806 ± 339	592 ± 181	513 ± 101
	Sim	1954 ± 117	1927 ± 124	587 ± 82	586 ± 44
Run length (µm)	Exp	2.12 ± 0.05	3.00 ± 0.06	2.18 ± 0.01	2.32 ± 0.03
	Sim	2.12 ± 0.13	2.80 ± 0.11	2.28 ± 0.15	2.65 ± 0.09

643

644   **Table S1:** Summary of velocity and run length for experiments (Exp) and simulations (Sim). Values are

645   mean ± s.d.

Variables	FLA8/8	KLP11/20
k_{on} (predicted)	4 /s	2.5 /s
$k_{off, 0}$	0.9193 /s	0.2716 /s
Unloaded velocity	1949 nm/s	592 nm/s
Stall force	6 pN	6 pN
k_s	0.06 pN/nm	0.06 pN/nm

646

647   **Table S2:** Summary of parameters used in the simulations. ($k_{off}(0)$ = velocity/run length).

648

649   **Supplementary movies**

650   **Supplementary movie 1**: Multiple-motor gliding filament assay of wild type FLA8/10. The

651   video is sped up 6X. Scale bar: 2 µm.

652   **Supplementary movie 2:** Colocalized assay of FLA8/8-FLA8/8 DNA hybrid. Top and

653   middle channels represent individual motors tagged with SNAP[488] and SNAP[647] dyes

654   respectively. The combined signal is shown in the bottom channel. The video is sped up

655   6X. Scale bar: 2 µm.

656   **Supplementary movie 3:** Colocalized assay of KLP11/20-KLP11/20 DNA hybrid. Top

657   and middle channels represent individual motors tagged with SNAP[488] and SNAP[647] dyes

658 respectively. The combined signal is shown in the bottom channel. The video is sped up

659 6X. Scale bar: 2 μm.

660 **Supplementary movie 4:** Movie shows a replication of an experimental movie of a

661 FLA8/8-FLA8/8 DNA hybrid using data from the simulation. Model convolution is utilized

662 with a Gaussian point spread function with a standard deviation of 300 nm. The top and

663 middle channels represent individual motors tagged with SNAP[488] and SNAP[647] dyes,

664 respectively. The combined signal is shown in the bottom channel. Scale bar: 2 μm.

665 **Supplementary movie 5:** Movie shows a replication of an experimental movie of a

666 KLP11/20-KLP11/20 DNA hybrid using data from the simulation. Model convolution is

667 utilized with a Gaussian point spread function with a standard deviation of 300 nm. The

668 top and middle channels represent individual motors tagged with SNAP[488] and SNAP[647]

669 dyes, respectively. The combined signal is shown in the bottom channel. Scale bar: 2 μm.

670

671 **References:**

672 1. Rosenbaum, J.L., and Witman, G.B. (2002). Intraflagellar transport. Nature reviews. Molecular cell
673   biology *3*, 813-825.

674 2. Scholey, J.M. (2003). Intraflagellar transport. Annual review of cell and developmental biology *19*,
675   423-443.

676 3. Laib, J.A., Marin, J.A., Bloodgood, R.A., and Guilford, W.H. (2009). The reciprocal coordination and
677   mechanics of molecular motors in living cells. Proceedings of the National Academy of Sciences of
678   the United States of America *106*, 3190-3195.

679 4. Cole, D.G., Diener, D.R., Himelblau, A.L., Beech, P.L., Fuster, J.C., and Rosenbaum, J.L. (1998).
680   Chlamydomonas kinesin-II-dependent intraflagellar transport (IFT): IFT particles contain proteins
681   required for ciliary assembly in Caenorhabditis elegans sensory neurons. The Journal of cell
682   biology *141*, 993-1008.

683 5. Badano, J.L., Mitsuma, N., Beales, P.L., and Katsanis, N. (2006). The ciliopathies: an emerging
684   class of human genetic disorders. Annual review of genomics and human genetics *7*, 125-148.

685 6. Nigg, E.A., and Raff, J.W. (2009). Centrioles, centrosomes, and cilia in health and disease. Cell
686   *139*, 663-678.

687 7. Pan, J., Wang, Q., and Snell, W.J. (2005). Cilium-generated signaling and cilia-related disorders.
688   Laboratory investigation; a journal of technical methods and pathology *85*, 452-463.

689 8. Scholey, J.M., and Anderson, K.V. (2006). Intraflagellar transport and cilium-based signaling. Cell
690   *125*, 439-442.

691   9.   Anvarian, Z., Mykytyn, K., Mukhopadhyay, S., Pedersen, L.B., and Christensen, S.T. (2019).
692   Cellular signalling by primary cilia in development, organ function and disease. Nature Reviews
693   Nephrology *15*, 199-219.

694   10.   Bisgrove, B.W., and Yost, H.J. (2006). The roles of cilia in developmental disorders and disease.
695   *133*, 4131-4143.

696   11.   Blacque, O.E., and Leroux, M.R. (2006). Bardet-Biedl syndrome: an emerging pathomechanism of
697   intracellular transport. Cellular and molecular life sciences : CMLS *63*, 2145-2161.

698   12.   Pazour, G.J., and Rosenbaum, J.L. (2002). Intraflagellar transport and cilia-dependent diseases.
699   Trends in cell biology *12*, 551-555.

700   13.   Kozminski, K.G., Johnson, K.A., Forscher, P., and Rosenbaum, J.L. (1993). A motility in the
701   eukaryotic flagellum unrelated to flagellar beating. Proceedings of the National Academy of
702   Sciences of the United States of America *90*, 5519-5523.

703   14.   Cole, D.G., Chinn, S.W., Wedaman, K.P., Hall, K., Vuong, T., and Scholey, J.M. (1993). Novel
704   heterotrimeric kinesin-related protein purified from sea urchin eggs. Nature *366*, 268-270.

705   15.   Kozminski, K.G., Beech, P.L., and Rosenbaum, J.L. (1995). The Chlamydomonas kinesin-like
706   protein FLA10 is involved in motility associated with the flagellar membrane. The Journal of cell
707   biology *131*, 1517-1527.

708   16.   Pazour, G.J., Dickert, B.L., and Witman, G.B. (1999). The DHC1b (DHC2) isoform of cytoplasmic
709   dynein is required for flagellar assembly. The Journal of cell biology *144*, 473-481.

710   17.   Porter, M.E., Bower, R., Knott, J.A., Byrd, P., and Dentler, W. (1999). Cytoplasmic dynein heavy
711   chain 1b is required for flagellar assembly in Chlamydomonas. Molecular biology of the cell *10*,
712   693-712.

713   18.   Signor, D., Rose, L.S., and Scholey, J.M. (2000). Analysis of the roles of kinesin and dynein motors
714   in microtubule-based transport in the Caenorhabditis elegans nervous system. Methods (San
715   Diego, Calif.) *22*, 317-325.

716   19.   Signor, D., Wedaman, K.P., Rose, L.S., and Scholey, J.M. (1999). Two heteromeric kinesin
717   complexes in chemosensory neurons and sensory cilia of Caenorhabditis elegans. Molecular
718   biology of the cell *10*, 345-360.

719   20.   Wedaman, K.P., Meyer, D.W., Rashid, D.J., Cole, D.G., and Scholey, J.M. (1996). Sequence and
720   submolecular localization of the 115-kD accessory subunit of the heterotrimeric kinesin-II
721   (KRP85/95) complex. The Journal of cell biology *132*, 371-380.

722   21.   Signor, D., Wedaman, K.P., Orozco, J.T., Dwyer, N.D., Bargmann, C.I., Rose, L.S., and Scholey,
723   J.M. (1999). Role of a class DHC1b dynein in retrograde transport of IFT motors and IFT raft
724   particles along cilia, but not dendrites, in chemosensory neurons of living Caenorhabditis elegans.
725   The Journal of cell biology *147*, 519-530.

726   22.   Mitchell, D.R. (2007). The evolution of eukaryotic cilia and flagella as motile and sensory
727   organelles. Advances in experimental medicine and biology *607*, 130-140.

728   23.   Scholey, J.M. (2013). Kinesin-2: a family of heterotrimeric and homodimeric motors with diverse
729   intracellular transport functions. Annual review of cell and developmental biology *29*, 443-469.

730   24.   Gilbert, S.P., Guzik-Lendrum, S., and Rayment, I. (2018). Kinesin-2 motors: Kinetics and
731   biophysics. The Journal of biological chemistry *293*, 4510-4518.

732   25.   Mueller, J., Perrone, C.A., Bower, R., Cole, D.G., and Porter, M.E. (2005). The FLA3 KAP subunit
733   is required for localization of kinesin-2 to the site of flagellar assembly and processive anterograde
734   intraflagellar transport. Molecular biology of the cell *16*, 1341-1354.

735   26.   Sarpal, R., Todi, S.V., Sivan-Loukianova, E., Shirolikar, S., Subramanian, N., Raff, E.C., Erickson,
736   J.W., Ray, K., and Eberl, D.F. (2003). Drosophila KAP interacts with the kinesin II motor subunit
737   KLP64D to assemble chordotonal sensory cilia, but not sperm tails. Current biology : CB *13*, 1687-
738   1696.

739   27.   Snow, J.J., Ou, G., Gunnarson, A.L., Walker, M.R., Zhou, H.M., Brust-Mascher, I., and Scholey,
740   J.M. (2004). Two anterograde intraflagellar transport motors cooperate to build sensory cilia on C.
741   elegans neurons. Nature cell biology *6*, 1109-1113.

742   28.   Teng, J., Rai, T., Tanaka, Y., Takei, Y., Nakata, T., Hirasawa, M., Kulkarni, A.B., and Hirokawa, N.
743   (2005). The KIF3 motor transports N-cadherin and organizes the developing neuroepithelium.
744   Nature cell biology *7*, 474-482.

745   29.   Brunnbauer, M., Mueller-Planitz, F., Kosem, S., Ho, T.H., Dombi, R., Gebhardt, J.C., Rief, M., and
746   Okten, Z. (2010). Regulation of a heterodimeric kinesin-2 through an unprocessive motor domain
747   that is turned processive by its partner. Proceedings of the National Academy of Sciences of the
748   United States of America *107*, 10460-10465.

749   30.   Pan, X., Ou, G., Civelekoglu-Scholey, G., Blacque, O.E., Endres, N.F., Tao, L., Mogilner, A.,
750   Leroux, M.R., Vale, R.D., and Scholey, J.M. (2006). Mechanism of transport of IFT particles in C.
751   elegans cilia by the concerted action of kinesin-II and OSM-3 motors. The Journal of cell biology
752   *174*, 1035-1045.

753   31.   Stepp, W.L., Merck, G., Mueller-Planitz, F., and Okten, Z. (2017). Kinesin-2 motors adapt their
754   stepping behavior for processive transport on axonemes and microtubules. EMBO reports *18*,
755   1947-1956.

756   32.   Andreasson, J.O., Shastry, S., Hancock, W.O., and Block, S.M. (2015). The Mechanochemical
757   Cycle of Mammalian Kinesin-2 KIF3A/B under Load. Current biology : CB *25*, 1166-1175.

758   33.   Tuma, M.C., Zill, A., Le Bot, N., Vernos, I., and Gelfand, V. (1998). Heterotrimeric kinesin II is the
759   microtubule motor protein responsible for pigment dispersion in Xenopus melanophores. The
760   Journal of cell biology *143*, 1547-1558.

761   34.   Yamazaki, H., Nakata, T., Okada, Y., and Hirokawa, N. (1995). KIF3A/B: a heterodimeric kinesin
762   superfamily protein that works as a microtubule plus end-directed motor for membrane organelle
763   transport. The Journal of cell biology *130*, 1387-1399.

764   35.   Stepanek, L., and Pigino, G. (2016). Microtubule doublets are double-track railways for intraflagellar
765   transport trains. Science (New York, N.Y.) *352*, 721-724.

766   36.   Iomini, C., Babaev-Khaimov, V., Sassaroli, M., and Piperno, G. (2001). Protein particles in
767   Chlamydomonas flagella undergo a transport cycle consisting of four phases. The Journal of cell
768   biology *153*, 13-24.

769   37.   Prevo, B., Mangeol, P., Oswald, F., Scholey, J.M., and Peterman, E.J. (2015). Functional
770   differentiation of cooperating kinesin-2 motors orchestrates cargo import and transport in C.
771   elegans cilia. Nature cell biology *17*, 1536-1545.

772   38.   Jordan, M.A., Diener, D.R., Stepanek, L., and Pigino, G. (2018). The cryo-EM structure of
773   intraflagellar transport trains reveals how dynein is inactivated to ensure unidirectional anterograde
774   movement in cilia. Nature cell biology *20*, 1250-1255.

775   39.   Mohamed, M.A.A., Stepp, W.L., and Okten, Z. (2018). Reconstitution reveals motor activation for
776   intraflagellar transport. Nature *557*, 387-391.

777   40.   Imanishi, M., Endres, N.F., Gennerich, A., and Vale, R.D. (2006). Autoinhibition regulates the
778   motility of the C. elegans intraflagellar transport motor OSM-3. The Journal of cell biology *174*, 931-
779   937.

780   41.   Cole, D.G. (1999). Kinesin-II, the heteromeric kinesin. Cellular and molecular life sciences : CMLS
781   *56*, 217-226.

782   42.   Stock, M.F., Guerrero, J., Cobb, B., Eggers, C.T., Huang, T.G., Li, X., and Hackney, D.D. (1999).
783   Formation of the compact conformer of kinesin requires a COOH-terminal heavy chain domain and
784   inhibits microtubule-stimulated ATPase activity. The Journal of biological chemistry *274*, 14617-
785   14623.

786   43.   Coy, D.L., Hancock, W.O., Wagenbach, M., and Howard, J. (1999). Kinesin's tail domain is an
787   inhibitory regulator of the motor domain. Nature cell biology *1*, 288-292.

788   44.   Friedman, D.S., and Vale, R.D. (1999). Single-molecule analysis of kinesin motility reveals
789   regulation by the cargo-binding tail domain. Nature cell biology *1*, 293-297.

790   45.   Ou, G., Blacque, O.E., Snow, J.J., Leroux, M.R., and Scholey, J.M. (2005). Functional coordination
791   of intraflagellar transport motors. Nature *436*, 583-587.

792   46.   Milic, B., Andreasson, J.O.L., Hogan, D.W., and Block, S.M. (2017). Intraflagellar transport velocity
793   is governed by the number of active KIF17 and KIF3AB motors and their motility properties under
794   load. Proceedings of the National Academy of Sciences of the United States of America *114*,
795   E6830-e6838.

796   47.   England, C.G., Luo, H., and Cai, W. (2015). HaloTag technology: a versatile platform for biomedical
797   applications. Bioconjugate chemistry *26*, 975-986.

798   48.   Urh, M., and Rosenberg, M. (2012). HaloTag, a Platform Technology for Protein Analysis. Current
799   chemical genomics *6*, 72-78.

800   49.   Arpag, G., Norris, S.R., Mousavi, S.I., Soppina, V., Verhey, K.J., Hancock, W.O., and Tuzel, E.
801   (2019). Motor Dynamics Underlying Cargo Transport by Pairs of Kinesin-1 and Kinesin-3 Motors.
802   Biophys J *116*, 1115-1126.

803   50.   Brunnbauer, M.D. (2012). Mechanische Untersuchungen heterodimerer Kinesin-2 Motoren. PHD

804   thesis.

805